

Optical Constants of Ices Important to Planetary Science From Laboratory Reflectance Spectroscopy

S.C. TEGLER¹,¹ W.M. GRUNDY^{2,1},¹ M.J. LOEFFLER,¹ P.D. TRIBBETT,³ J. HANLEY,^{2,1} A.V. JASKO,^{4,5,1}
H. DAWSON,^{6,7,1} A.N. MORGAN,¹ K.J. KOGA,¹ A.O. MADDEN-WATSON,¹ M.D. GOMEZ,¹ J.K. STECKLOFF,⁸
G.E. LINDBERG,¹ S.P. TAN,⁸ S.M. RAPOSA,¹ A.E. ENGLE,¹ C.L. THEIEBERGER¹,¹ AND D.E. TRILLING¹

¹*Northern Arizona University*

²*Lowell Observatory*

³*NASA Goddard Spaceflight Center*

⁴*University of Rochester*

⁵*Case Western Reserve University*

⁶*Washington University*

⁷*Purdue University*

⁸*Planetary Science Institute*

ABSTRACT

Laboratory-derived optical constants are essential for identifying ices and measuring their relative abundances on Solar System objects. Almost all optical constants of ices important to planetary science come from experiments with transmission geometries. Here, we describe our new experimental setup and the modification of an iterative algorithm in the literature to measure the optical constants of ices from experiments with reflectance geometries. We apply our techniques to CH₄ ice and H₂O ice samples and find good agreement between our values and those in the literature, except for one CH₄ band in the literature that likely suffers from saturation. The work we present here demonstrates that labs with reflectance geometries can generate optical constants essential for the proper analysis of near- and mid-infrared spectra of outer Solar System objects such as those obtained with the James Webb Space Telescope.

1. INTRODUCTION

Optical constants are essential for identifying and measuring the abundances of molecular ices on the surfaces of Solar System objects. Specifically, they are necessary inputs for radiative transfer models that generate synthetic spectra (Hapke 1993; Shkuratov et al. 1999). Comparison of these synthetic spectra to telescope or spacecraft spectra results in the identification and abundance measurements of ices on Solar System bodies. For examples, see Cruikshank et al. (1998); Dumas et al. (2007); Merlin et al. (2010); Tegler et al. (2012); Grundy et al. (2020).

Laboratory techniques to measure the optical constants of molecular ices date back decades. One of the earliest experiments of importance to planetary science was by Bergren et al. (1978), where they established the experimental and iterative computational techniques of extracting optical constants from a single infrared transmission spectrum of a thin-film sample. Subsequent experiments to measure optical constants of importance to planetary science include works by Hagen et al. (1981), Hudgins et al. (1993), Hansen (1997), and Mastrapa et al. (2008, 2009).

Recently, Gerakines & Hudson (2020) made significant computational improvements to the technique first put forward by Bergren et al. (1978) and Hagen et al. (1981). In addition, they made the point that the literature sometimes exhibits large differences in optical constants for the same material, which may be due to either subtleties in the experimental techniques or differences in the algorithms to extract the optical constants. They further point out that it is impossible to sort out the causes for the differences because few published results provide digital access to the original laboratory data, the algorithm to extract the optical constants from the data, and the resulting optical

constants. Gerakines and Hudson made their experimental data, algorithm, and resulting optical constants for dozens of ices available on their website¹ and Zenodo².

It is possible to obtain optical constants of thin films from transmission or reflectance geometries (Tolstoy et al. 2003). In transmission geometry, a vapor deposits as ice onto a cold transparent substrate. The spectrometer beam, nearly normal to the surface of the sample, passes through the ice, then the substrate, and then often through a thinner layer of ice on the back side of the substrate on its way to the detector. In reflectance geometry, a vapor deposits ice onto a highly reflective surface such as gold. The spectrometer beam is likely at an oblique angle to the surface of the ice sample. Part of the beam reflects off the surface of the ice back to the detector. The rest of the beam passes through the sample, reflects off the substrate, passes through the sample again, and finally travels onto the detector. The two parts of the beam recombine (out of phase) and create channel fringes in the spectrum. Previous optical constant work mostly uses transmission spectroscopy as the mathematics to extract optical constants from transmission spectra is simpler than the mathematics to extract optical constants from reflectance spectra. For instance, in reflectance geometry the spectrometer beam typically is not perpendicular to the ice surface, making it necessary to account for the S and P polarization states and work with more complex Fresnel coefficients.

Although extraction of optical constants is mathematically complex for reflection spectroscopy, it has advantages. First, we don't have to account for ice on the backside of the substrate as is necessary for transmission geometry. Second, it's possible to irradiate ices with electrons or ions in reflectance geometry and study the resulting solid-state chemistry. Irradiation of transparent substrates may result in electrostatic charging and changes in the substrate properties (Clark & Crawford 1973; Teolis et al. 2007). Third, it is possible to use a quartz-crystal micro-balance (QCM) as the substrate in reflectance geometry and obtain information about the density of the ice (Westley et al. 1998; Loeffler et al. 2006) and its vapor pressure (Grundy et al. 2023). Because of these advantages, we decided to modify the algorithm by Gerakines & Hudson (2020) for transmission geometry to work in reflection geometry.

Below, we describe our experimental setup and algorithm to measure the optical constants of ices in reflectance geometry, applying the algorithm to two ices of importance to planetary science, CH₄ and H₂O.

2. EXPERIMENTAL SETUP

We performed experiments in the Astrophysical Materials Laboratory at Northern Arizona University. We pumped on our vacuum chamber with an Agilent TwisTorr 305 FS turbomolecular pump backed up by an Agilent Varian DS302 dual-stage rotary vane roughing pump. The base pressure in the chamber at room temperature was typically 1 to 2 x 10⁻⁸ torr. Cryocooling allowed us to reach pressures as low as 2 x 10⁻⁹ torr. We used an Agilent variable leak valve (model number 951-5106) to transfer samples from the reservoir to the vacuum chamber. We background deposited samples onto the substrate, while monitoring the pressure (~ 10⁻⁶ torr) with an INFICON Bayard-Alpert Pirani combination gauge sensor (model number BPG-400).

We deposited our samples onto an INFICON IC6 optically-flat, gold-plated, quartz-crystal microbalance (QCM) attached to an Advanced Research Systems (ARS) DE-204PB two-stage closed-cycle helium cold head hanging vertically into the vacuum chamber (Figure 1). We measured the temperatures of a sample on the quartz crystal using two temperature-sensitive diodes. The temperature was controlled with a 50 Ω heater wrapped around the cold tip and a Lake Shore temperature controller (model 355). We used a copper QCM mount and copper strap to maximize the thermal conductivity between the cold tip and the gold-plated quartz crystal. We were able to cool samples as low as 10 K.

We used a three-laser setup to measure the index of refraction of the sample at the wavelength of the lasers and the thickness of the sample. We placed two blue lasers of wavelengths 0.407 μm and 0.405 μm at angles $\theta_1 = 3.7^\circ \pm 1.0^\circ$

¹ <https://science.gsfc.nasa.gov/691/cosmicice/constants.html>

² <https://doi.org/10.5281/zenodo.4429276>

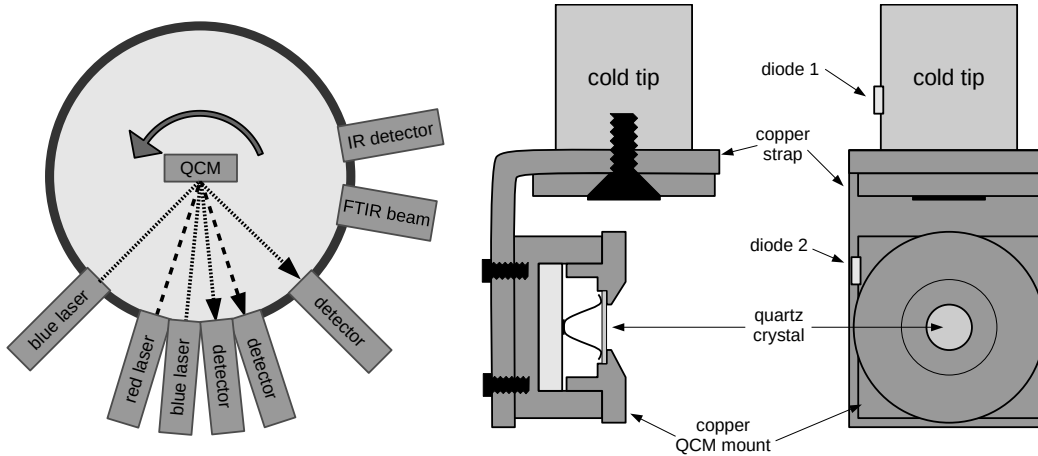


Figure 1. The left figure is a view of QCM from above showing its location relative to the lasers, detectors, and FTIR beam in our system. The center figure is a side view of the QCM. The right figure is a face-on view of the QCM. The center and right figures show the cold head, two diodes for temperature measurements, copper strap, and QCM mount. Ice is deposited on the gold-plated quartz crystal. For clarity, wiring and indium foil to improve thermal conduction between the copper strap and the copper QCM mount are not shown.

and $\theta_2 = 45.2^\circ \pm 1.0^\circ$ to the normal of the quartz-crystal surface while we grew an ice sample. We computed the index of refraction using

$$n_{blue} = \sqrt{\frac{\sin^2\theta_2 - \left(\frac{t_1}{t_2}\right)^2 \sin^2\theta_1}{1 - \left(\frac{t_1}{t_2}\right)^2}} \quad (1)$$

where t_1 and t_2 , were the oscillation periods of the laser signals for the narrow-angle laser and the wide-angle laser, respectively, during deposition of the ice sample (Tempelmeyer & Mills 1968; Satorre et al. 2008; Romanescu et al. 2010; Loeffler et al. 2016).

We calculated the thickness, h , of the sample in μm from the number of fringes in the narrow-angle laser signal, N_1 , using

$$h = \frac{N_1 \lambda}{2\sqrt{n_{blue}^2 - \sin^2\theta_1}} \quad (2)$$

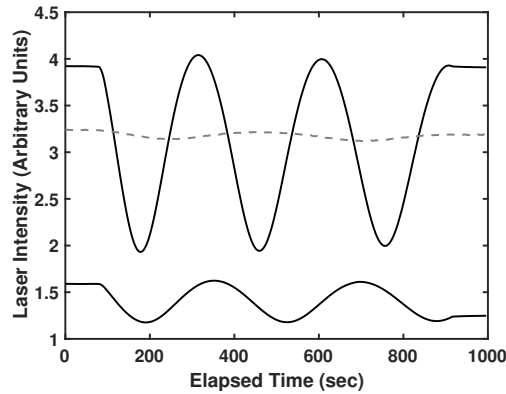
(Heavens 1991) where λ is the wavelength of the blue laser ($0.407 \mu\text{m}$). For the two CH_4 experiments we report on here, the thicknesses were $0.44 \mu\text{m}$ and $1.54 \mu\text{m}$. For the H_2O experiment, the thickness was $0.23 \mu\text{m}$.

Our techniques for measuring t_1/t_2 and N_1 are different from what is published in the literature. First, we used blue lasers rather than red lasers because blue lasers give more fringes and deeper fringes than red lasers. In Figure 2a, we compare the fringes from the two blue lasers at $\theta_1 = 3.7^\circ \pm 1.0^\circ$ (top black line) and $\theta_2 = 45.2^\circ \pm 1.0^\circ$ (bottom black line) to the fringes from a third red laser at near-normal incidence to the sample surface (dashed black line). Second, we used the QCM to change the units on the x-axis from elapsed time in seconds as seen in Figure 2a to the fraction of full deposition, x , as seen in Figure 2b. Specifically, the QCM measured a frequency that depended on the deposited mass, where f_1 was the frequency prior to deposition and f_2 was the frequency after deposition. At each time step, i , we computed the fraction of full deposition as $x = (f_1 - f(i))/(f_1 - f_2)$. The conversion enabled us to remove any effects due to a variable deposition rate. Third, we determined the ratio of laser signal periods, t_1/t_2 ,

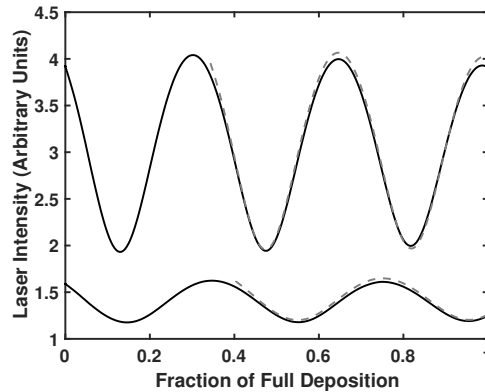
103 by measuring the number of fringes in each laser signal, N_1 and N_2 . The values $1/N_1$ and $1/N_2$ gave the periods of
 104 the signals because we plotted each signal against the fraction of full deposition that ranged in value from 0 to 1. To
 105 determine the number of fringes for the first laser signal, we repeatedly plotted the original signal (x , laser-intensity₁),
 106 and the original signal shifted by $1/N$ ($x + 1/N$, laser-intensity₁) until we found the value of N that resulted in the
 107 best over-plot of the shifted signal on the original signal. We repeated the process for the second laser signal. We show
 108 the best-shifted signals in Figure 2b as dashed black lines. The ratio of the number of fringes gave us t_1/t_2 ,

$$109 \quad \frac{t_1}{t_2} = \frac{N_2}{N_1}. \quad (3)$$

110



(a)



(b)

Figure 2. Laser interferometry. **a)** Intensities of lasers vs. elapsed time of deposition. The two blue lasers at $\theta_1 = 3.7^\circ$ (top black line) and $\theta_2 = 45.2^\circ$ (bottom black line) have more fringes and deeper fringes compared to a red laser at near-normal incidence to the sample surface (dashed black line). **b)** Intensities of two blue lasers vs. fraction of full deposition allow us to remove the effects of a variable deposition rate. Original laser signals shifted by one period (dashed black lines) enable us to determine the periods of the laser signals.

111 We used the QCM to measure the density, ρ , of our ice sample in g cm^{-3} . Specifically, the QCM measured the
 112 resonance frequency of the quartz-crystal prior to the deposition, f_1 , and at the end of the deposition, f_2 , in Hz.
 113 Combining these measured frequencies with our thickness measurement above, we computed the density from

$$\rho = \frac{C}{h} \left(\frac{1}{f_2} - \frac{1}{f_1} \right) \quad (4)$$

where $C = 4.417 \times 10^5 \text{ Hz g cm}^{-2}$ depends on the density and frequency constant of an AT-cut quartz-crystal (Lu & Lewis 1972).

We used a Thermo-Nicolet iS50 Fourier transform infrared (FTIR) spectrometer to generate an external beam. Gold-coated parabolic mirrors focused the beam at an incidence angle of 8.5 degrees to the normal of the sample and upon reflection focused the beam onto a Mercury Cadmium Telluride type A (MCT-A) detector. All experiments covered a wavenumber, $\tilde{\nu}$, (wavelength) range between 8000 cm^{-1} ($1.25 \mu\text{m}$) and 1000 cm^{-1} ($10 \mu\text{m}$) at a resolution of 0.5 cm^{-1} . We averaged 125 scans for each sample and reference (bare substrate) spectrum.

3. REFLECTANCE MODEL

Extraction of optical constants from a reflectance spectrum requires a model that simulates the experimental reflectance data. Teolis et al. (2007) devised such a model; however, they focused on band strengths rather than optical constants and did not publish their code. Here, we describe our reflectance model. We assign variables consistent with the Gerakines & Hudson (2020) transmission model. In particular, we define the optical constants of the thin film sample as $m_1(\tilde{\nu}) = n_1(\tilde{\nu}) - ik_1(\tilde{\nu})$, where n_1 is the real-part and k_1 is the imaginary-part. In the model, the light at wavenumber $\tilde{\nu}$ in a vacuum is incident on the surface of the thin film of thickness h at an angle ϕ_0 to the surface normal. Light from the FTIR reflects and refracts at the interfaces on its way to the detector as shown in Figure 3. We denote quantities associated with the vacuum, film, and substrate with the subscripts 0, 1, and 2, respectively. Because the incident light is not normal to the surface, we must account for the S and P polarization states. We assume unpolarized light and so we assign equal weights to the P- and S-states, where the P-state is the component of light that has its electric field parallel to the ice surface and the S-state is the component that has its electric field perpendicular to the surface.

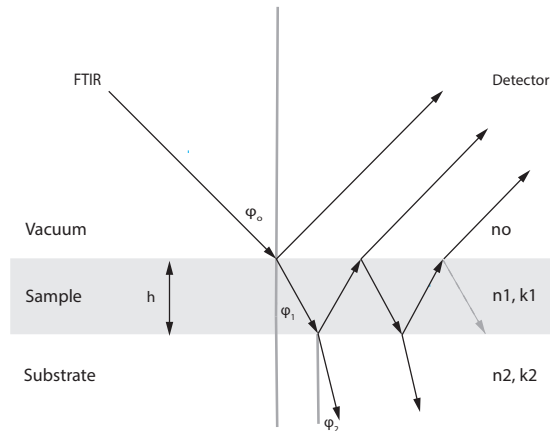


Figure 3. Quantities in the reflection model and the path of light from the FTIR, through the sample, and onto the detector.

Because we need to divide the experimental sample spectrum by the reference spectrum to remove instrumental effects, our model computes the reflectance spectrum from the ice-covered substrate divided by the reflectance spectrum from the bare substrate, *i.e.*, the reflectance ratio, R , given by

$$R = \frac{R^P + R^S}{|r_{20}^P|^2 + |r_{20}^S|^2} \quad (5)$$

140

141 where

142

$$R^P = \left| \frac{r_1^P + r_2^P e^{-2i\delta_1}}{1 + r_1^P r_2^P e^{-2i\delta_1}} \right|^2 \quad (6)$$

143

144 and

145

$$R^S = \left| \frac{r_1^S + r_2^S e^{-2i\delta_1}}{1 + r_1^S r_2^S e^{-2i\delta_1}} \right|^2 \quad (7)$$

146

147 The lowercase r symbols represent the Fresnel coefficients. The coefficient r_1^P and r_1^S represent the amplitude of P-state
148 light and S-state light reflected at the vacuum-ice interface and are given by

149

$$r_1^P = \frac{m_0 \cos \phi_1 - m_1 \cos \phi_0}{m_0 \cos \phi_1 + m_1 \cos \phi_0}. \quad (8)$$

150

151

$$r_1^S = \frac{m_0 \cos \phi_0 - m_1 \cos \phi_1}{m_0 \cos \phi_0 + m_1 \cos \phi_1}. \quad (9)$$

152

153 The coefficient r_2^P and r_2^S represent the amplitude of P-state light and S-state light reflected at the ice-substrate
154 interface and are given by

155

$$r_2^P = \frac{m_1 \cos \phi_2 - m_2 \cos \phi_1}{m_1 \cos \phi_2 + m_2 \cos \phi_1}. \quad (10)$$

156

157

$$r_2^S = \frac{m_1 \cos \phi_1 - m_2 \cos \phi_2}{m_1 \cos \phi_1 + m_2 \cos \phi_2}. \quad (11)$$

158

159 The coefficients r_{20}^P and r_{20}^S represent the amplitude of P-state light and S-state light reflected at the vacuum-substrate
160 interface and are given by

161

$$r_{20}^P = \frac{m_0 \cos \phi_{20} - m_2 \cos \phi_0}{m_0 \cos \phi_{20} + m_2 \cos \phi_0}. \quad (12)$$

162

163

$$r_{20}^S = \frac{m_0 \cos \phi_0 - m_2 \cos \phi_{20}}{m_0 \cos \phi_0 + m_2 \cos \phi_{20}}. \quad (13)$$

164

165 It is important to recognize that m_0 , m_1 , and m_2 are the optical constants for vacuum, the ice film, and substrate,
 166 respectively, and are complex functions given by

$$167 \quad m_0 = n_0 - ik_0 \quad (14)$$

$$169 \quad m_1 = n_1(\tilde{\nu}) - ik_1(\tilde{\nu}) \quad (15)$$

$$171 \quad m_2 = n_2(\tilde{\nu}) - ik_2(\tilde{\nu}) \quad (16)$$

173 The optical constants $n_0 = 1$ and $k_0 = 0$ are for vacuum. The optical constants n_2 and k_2 are for the gold substrate
 174 (Babar & Weaver 2015).

175 The trigonometric values $\cos\phi_1$, $\cos\phi_2$, $\cos\phi_{20}$ come from the complex version of Snell's Law and are given by

$$176 \quad \cos\phi_1 = \left(1 - \frac{\sin^2\phi_0}{n_1^2 - k_1^2 - 2in_1k_1}\right)^{1/2} \quad (17)$$

$$178 \quad \cos\phi_2 = \left(1 - \frac{n_1^2 - k_1^2 - 2n_1k_1 \sin^2\phi_1}{n_2^2 - k_2^2 - 2n_2k_2}\right)^{1/2} \quad (18)$$

$$180 \quad \cos\phi_{20} = \left(1 - \frac{\sin^2\phi_0}{n_2^2 - k_2^2 - 2n_2k_2}\right)^{1/2} \quad (19)$$

182 Finally, δ_1 is the change in phase of the beam on traversing the film and is given by

$$183 \quad \delta_1 = 2\pi\tilde{\nu}m_1h\cos\phi_1 \quad (20)$$

185 See Heavens (1991) for derivations of Equations 6 – 13 and 20.

4. ITERATIVE ALGORITHM

It is not possible to invert (5) and analytically solve for $n_1(\tilde{\nu})$ and $k_1(\tilde{\nu})$. Rather, the canonical approach, most recently described and modified by Gerakines & Hudson (2020), is to compare the model spectrum to the experimental spectrum and make iterative changes to the values of $n_1(\tilde{\nu})$ and $k_1(\tilde{\nu})$ in the model until the model spectrum closely approximates the experimental spectrum. We briefly outline the canonical method, while focusing on modifications we made to the Gerakines and Hudson Python code that is available on their website¹.

First, we collected the necessary inputs for the algorithm, *i.e.*, our measurements of h , n_{blue} , and the experimental reflectance ratio, R_{lab} , as well as the published optical constants for gold, $n_2(\tilde{\nu})$ and $k_2(\tilde{\nu})$, from Babar & Weaver (2015). Next, we set $n_1(\tilde{\nu}) = n_{blue}$ and $k_1(\tilde{\nu}) = 0$. Then, we used the reflectance model described in Section 3 to compute the first model spectrum, R . Just like Gerakines & Hudson (2020), we next computed a first improvement to k_1 using the Newton-Raphson root-finding method *i.e.*, Δk_1 , given by

$$\Delta k_1 = \frac{\ln R_{lab} - \ln R(n_1, k_1)}{(\partial \ln R / \partial k_1)|_{n_1, k_1}}. \quad (21)$$

Because of the complexity of R for reflectance at oblique incidence, we used a numerical approximation to the partial derivative in the denominator of (21). We note that the analytical expression used by Gerakines and Hudson for this partial derivative only applies to a transmission experiment at normal incidence. After replacing k_1 with $k_1 + \Delta k_1$, we used an approximation to a Kramers–Kronig relation to compute a new n_1 at each wavenumber $\tilde{\nu}_i$ of the spectrum,

$$n_1(\tilde{\nu}_i) \approx n_{blue} + \frac{2}{\pi} \int_{ir} \frac{\tilde{\nu} k_1(\tilde{\nu})}{\tilde{\nu}^2 - \tilde{\nu}_i^2} d\tilde{\nu}. \quad (22)$$

We note that if the ice has a strong absorption band between the wavelength of the blue laser and where the integration begins in (22), the approximation could break down. However, in our case, neither CH₄ nor H₂O discussed below has strong absorption bands in this region.

Next, we computed a second model R and compared it to R_{lab} . Then, we computed the fractional deviation between the model and experimental spectrum at each $\tilde{\nu}$,

$$\frac{|R_{lab} - R(n_1, k_1)|}{R_{lab}}. \quad (23)$$

We then recalculated new values of n_1 and k_1 using (21) and (22) and subsequent values of R and the fractional deviation. We repeated the process until the fractional deviation was $< 1.0 \times 10^{-5}$ at every $\tilde{\nu}$.

In short, we modified the Python code of Gerakines & Hudson (2020) to include the reflection physics in Section 3, gold optical constants for the substrate, and a numerical approximation to the denominator in (21). The rest of the code is the same as the Gerakines and Hudson code, and their Figure 2 provides a flow chart of the overall algorithm.

5. RESULTS

5.1. CH₄

In this section, we describe our measurements of n_{blue} , ρ , $n_1(\tilde{\nu})$, and $k_1(\tilde{\nu})$ for CH₄. In each experiment, we obtained a spectrum of the bare substrate and recorded the laser and QCM signals while we background deposited the CH₄-ice at 10 K.

Table 1. Index of Refraction and Density of Crystalline CH₄

Phase	T (K)	λ (nm)	n_{vis}	ρ (g cm ⁻³)	Ref
Crystal II	10	0.407	1.34 ± 0.02	0.49 ± 0.01	a
Crystal II	10	0.633	1.30	0.47	b
Crystal I	30	0.633	1.30	0.47	b
Crystal I	30	0.628	1.36	0.45	c

^aThis Work

^bSatorre et al. (2008)

^cMolpeceres et al. (2017)

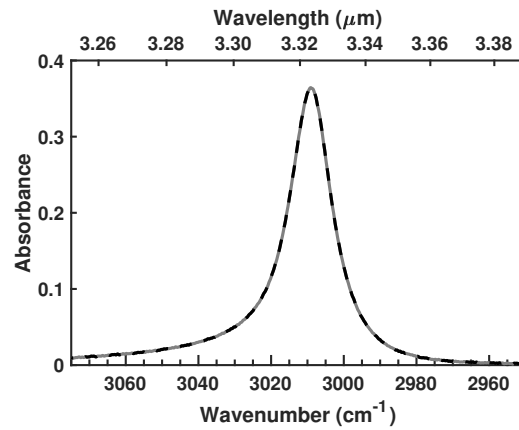
222 CH₄ ice has three different phases between 10 K and 30 K: amorphous, crystalline II, and crystalline I. Using profiles
 223 of the ν_4 band near 1300 cm⁻¹, Gerakines & Hudson (2015) showed the formation of amorphous CH₄ required a
 224 slow deposition rate at temperatures below 20 K, and crystalline II resulted from a fast deposition rate below 20 K.
 225 Warming crystalline II ice from 10 K to 30 K formed crystalline I ice.

226 In our experiments, we wanted to measure optical constants for crystalline I CH₄ and compare them to values reported
 227 by Gerakines & Hudson (2015). Using the same procedure as described in their work, we quickly deposited at 10 K
 228 obtaining n_{blue} and ρ . A spectrum of each sample at 10 K showed a ν_4 band with a double peak, confirming crystalline
 229 II ice. Next, we warmed the sample 4 K min⁻¹ to 30 K. The spectra showed a symmetric ν_4 band, confirming we had
 230 crystalline I ice

231 In Table 1, we present our measurements for the index of refraction and density of CH₄ compared to previous work.
 232 We measure $n_{blue} = 1.34 \pm 0.02$ for CH₄ deposited at 10 K. The uncertainty in n_{blue} is dominated by the uncertainty
 233 in our measurement of θ_2 . Given the scatter of the index of refraction values in the work of Satorre et al. (2008)
 234 (their Figure 3), we conclude our measurement for the index of refraction is consistent with their measurement. Our
 235 density measurement is $\rho = 0.49 \pm 0.01$ g cm⁻³ at 10 K. The uncertainty is the standard deviation of values from five
 236 experiments. From Table 1, we see our density measurement is in good agreement with Satorre.

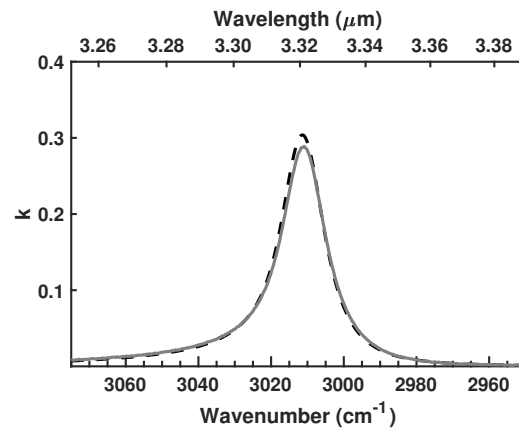
237 In Figure 4, we compare our measured spectrum to our best-fit model for the CH₄ ν_3 band at 3011 cm⁻¹. We make the
 238 comparison in absorbance, *i.e.*, $-\log_{10}(R_{sam}/R_{ref})$ to $-\log_{10}R$, where (R_{sam}/R_{ref}) is the sample spectrum divided
 239 by the reference spectrum (dashed black line) and R is the model spectrum from (5) (grey line). There is excellent
 240 agreement between the experimental and model spectra.

241 In Figure 5a and 5b, we plot the imaginary part of the optical constants, $k_1(\tilde{\nu})$, for the ν_3 (3011 cm⁻¹) and the ν_4 (1300
 242 cm⁻¹) vibrational modes (grey line). These k -values come from our reflection spectrum of a 0.44 μ m thick sample and
 243 the reflectance model described above. In addition, we over-plot k -values from Gerakines & Hudson (2020) (dashed
 244 black line) for a sample deposited at 10 K and warmed to 30 K. Despite the difference in reflection and transmission
 245 geometries, there is excellent agreement between the k -spectra. The agreement confirms consistent experimental and
 246 modeling procedures for both groups, as well as providing confidence in these k -values for radiation transfer modeling
 247 of outer Solar System objects.

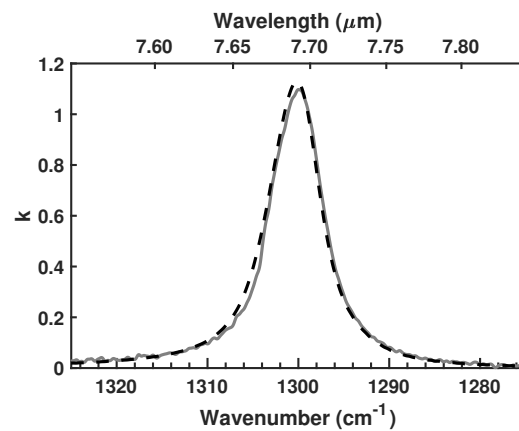


(b)

Figure 4. Comparison between experimental absorbance (dashed black line) and model (grey line) for the CH_4 ν_3 band at 3011 cm^{-1} .



(a)



(b)

Figure 5. Comparison between our k -values (grey lines) and Gerakines & Hudson (2020) k -values (dashed black lines) for CH_4 at 30 K. a) The ν_3 band at 3011 cm^{-1} . b) The ν_4 band at 1300 cm^{-1} .

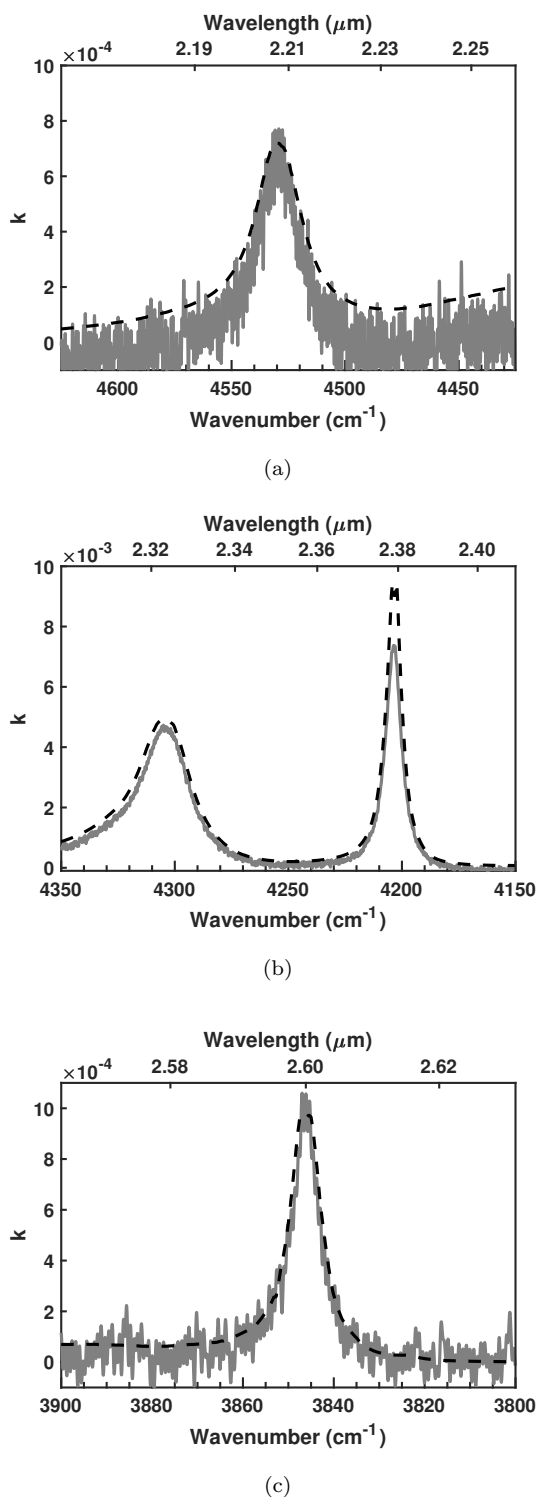


Figure 6. Comparison between our k -values (grey lines) and Grundy et al. (2002) k -values (dashed black lines) for CH_4 at 30 K. **a)** The $\nu_2 + \nu_3$ band at 4530 cm^{-1} . **b)** The $\nu_3 + \nu_4$ band at 4303 cm^{-1} and the $\nu_1 + \nu_4$ band at 4203 cm^{-1} . **c)** The $3\nu_4$ band at 3846 cm^{-1} .

248 In Figure 6a – 6c, we plot our k -values for a thicker $1.54 \mu\text{m}$ CH_4 sample so as to study the intrinsically weaker
 249 overtones and combination bands of CH_4 . We compare our k -values (grey lines) to the k -values of Grundy et al.
 250 (2002) (dashed black lines). Unsurprisingly, the Grundy values exhibit a much higher signal-to-noise ratio than our

values due to the much larger thicknesses of their samples. However, there is good agreement between the two sets of k -values. We note that the $\nu_2 + \nu_3$ band in Figure 6a is more than 1000 times weaker than the ν_4 band plotted in Figure 5b. In Figure 6b, we plot the k -values for the $\nu_3 + \nu_4$ band at 4303 cm^{-1} and the $\nu_1 + \nu_4$ band at 4203 cm^{-1} . We find good agreement between our values and the Grundy values for the $\nu_3 + \nu_4$ band; however, we find a significant disagreement in the $\nu_1 + \nu_4$ band. The double-peak at the top of the $\nu_1 + \nu_4$ band in the Grundy spectrum suggests saturation of the band. In Figure 6c, we plot the k -values for the $3\nu_4$ band at 3846 cm^{-1} . Again, we find good agreement between our values and the Grundy values, despite the much lower signal-to-noise of our much thinner sample. In summary, we find good agreement with the Grundy k -values, except for the $\nu_1 + \nu_4$ band at 4203 cm^{-1} where our thinner sample assures no saturation.

5.2. H_2O

Our experimental setup is capable of studying materials that are liquids at room temperature. Here, we describe our measurements of n_{blue} , ρ , $n_1(\tilde{\nu})$, and $k_1(\tilde{\nu})$ for crystalline H_2O .

Our sample preparation was as follows. We removed dissolved air in our purified liquid H_2O with a freeze-pump-thaw process. Because an initially cold amorphous H_2O sample heated past the amorphous–crystalline phase change at $\sim 135 \text{ K}$ can retain significant amounts of amorphous ice (Jenniskens et al. 1998), we deposited our samples at 150 K to ensure a crystalline sample.

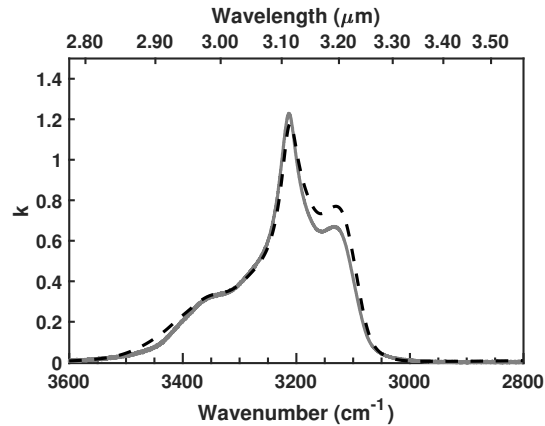
For the index of refraction, we measured $n_{blue} = 1.36 \pm 0.02$. The uncertainty in n_{blue} is dominated by the uncertainty in θ_2 . Hudgins et al. (1993) cited values of 1.26 to 1.35 in the literature for amorphous and crystalline H_2O and used a value of 1.32. Westley et al. (1998) measured 1.29 ± 0.01 that was independent of deposition temperature between 30 K and 140 K . Mastrapa et al. (2008, 2009) cited $n = 1.32$ at the wavelength of their laser from Hale & Querry (1973) for crystalline H_2O ; however, the reference is for liquid H_2O at 298 K .

For density, we measured $\rho = 0.95 \pm 0.01 \text{ g cm}^{-3}$. Narten et al. (1976) used x-ray diffraction data to measure $\rho = 0.94 \text{ g cm}^{-3}$ for amorphous ice at 77 K . Westley et al. (1998) measured $\rho = 0.82 \pm 0.01 \text{ g cm}^{-3}$ for thin films vapor deposited between 30 K and 140 K . Hobbs (1974) reported $\rho = 0.92 \text{ g cm}^{-3}$ for hexagonal ice.

H_2O bands span orders of magnitude in their absorption efficiency and so require a range of thicknesses to avoid saturation of the bands. We chose to study the feature near 3200 cm^{-1} ($3.1 \mu\text{m}$) because of its large absorption efficiency and importance to planetary science. The feature is such a strong absorber that it required a very thin sample corresponding to about one interference fringe, thereby preventing us from using the method described above for measuring the thickness of the sample. So, we used our average density, the initial and final QCM frequencies for depositing the thin sample, and re-arranged (4) to solve for thickness. We measured a sample thickness of $0.23 \mu\text{m}$. This technique was used by Loeffler et al. (2020) to measure the thicknesses of very thin H_2O samples. We cooled the sample from 150 K to 10 K and collected spectra at intervals of 10 K .

In Figure 7, we plot our k -values for the 3350 cm^{-1} ($2.99 \mu\text{m}$) ν_3 LO mode, 3200 cm^{-1} ($3.1 \mu\text{m}$) ν_3 TO mode, and the 3100 cm^{-1} ($3.2 \mu\text{m}$) ν_1 mode (grey line) and compare them to those of Mastrapa et al. (2009) (dashed black line). We found good agreement between the two sets of k -values for the 3350 cm^{-1} ($2.99 \mu\text{m}$) and 3200 cm^{-1} ($3.1 \mu\text{m}$) bands; however, there was a small difference between the k -values for the 3100 cm^{-1} ($3.2 \mu\text{m}$) band. Perhaps the small differences are due to Mastrapa computing k values from their transmission spectrum and then using the Kramers-Kronig relation to compute n rather than the iterative approach described here.

In Figure 8, we plot k -values for the 3350 cm^{-1} ($2.99 \mu\text{m}$), 3200 cm^{-1} ($3.1 \mu\text{m}$), and 3100 cm^{-1} ($3.2 \mu\text{m}$) bands of crystalline H_2O at temperatures of 150 K (dashed black line), 100 K (grey line), and 50 K (black line). As the temperature cools, the 3200 cm^{-1} ($3.1 \mu\text{m}$) band becomes stronger and shifts to smaller wavenumbers (larger wavelengths) and the 3100 cm^{-1} ($3.2 \mu\text{m}$) band becomes more pronounced in the spectrum. Similar behavior was seen for these bands in Figure 5 of Mastrapa et al. (2009).



(b)

Figure 7. Imaginary part of the optical constants, k , as a function of wavenumber and wavelength for crystalline H_2O at 50 K from this work (grey line) and [Mastrapa et al. \(2008\)](#) (dashed black line). The 3350 cm^{-1} ($2.99\text{ }\mu\text{m}$) ν_3 LO mode, 3200 cm^{-1} ($3.1\text{ }\mu\text{m}$) ν_3 TO mode, and the 3100 cm^{-1} ($3.2\text{ }\mu\text{m}$) ν_1 mode.

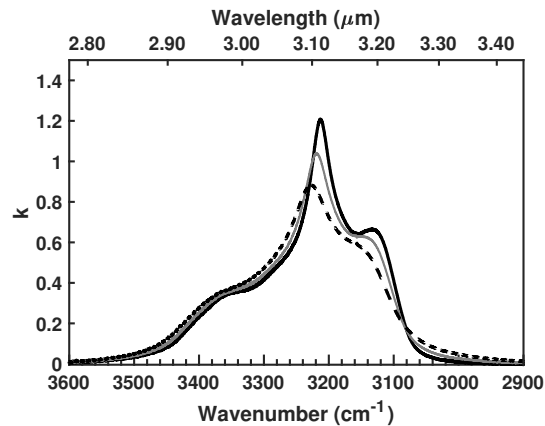


Figure 8. Imaginary part of the optical constants, k , as a function of wavenumber and wavelength for the 3350 cm^{-1} ($2.99\text{ }\mu\text{m}$) ν_3 LO mode, 3200 cm^{-1} ($3.1\text{ }\mu\text{m}$) ν_3 TO mode, and the 3100 cm^{-1} ($3.2\text{ }\mu\text{m}$) ν_1 mode of crystalline H_2O at 150 K (dashed black line), 100 K (grey line), and 50 K (black line).

6. CONCLUSIONS

We described our experimental setup and a modification of the algorithm by [Gerakines & Hudson \(2020\)](#) to compute optical constants from reflectance spectroscopy. We applied our experimental techniques and algorithm to CH_4 -ice at 30 K. We found good agreement with optical constants by [Gerakines & Hudson \(2020\)](#) and [Grundy et al. \(2002\)](#), except for the $\nu_1 + \nu_4$ band at 4203 cm^{-1} where their band profile suggests saturation. The overall good agreement with the literature gives us confidence in our experimental techniques and our modification of the Gerakines and Hudson algorithm. We applied the modified algorithm to our experiments on crystalline H_2O ice at 50 K. The resulting k -values for the 3200 cm^{-1} ($3.1\text{ }\mu\text{m}$) feature compared well with [Mastrapa et al. \(2008\)](#).

We demonstrated that our experimental setup and modifications to the [Gerakines & Hudson \(2020\)](#) algorithm are capable of computing optical constants consistent with what is published in the literature. These tools will be of use in computing optical constants essential for modeling the near- and mid-infrared spectra of outer Solar System objects obtained with the James Webb Space Telescope.

306 NASA SSW grant 80NSSC19K0556 provided support for this work. The Arizona Board of Regents Technology
 307 Research Initiative Fund (TRIF) provided funds for the purchase of equipment. The National Science Foundation
 308 Research Experience for Undergraduates Program at Northern Arizona University (NSF Award #1950901) and the
 309 Northern Arizona University Division of the Arizona Space Grant Consortium NASA provided financial support for
 310 the undergraduate researchers. We thank Dr. Perry Gerakines for helpful discussions about his algorithm.

REFERENCES

- 311 Babar, S., & Weaver, J. H. 2015, *ApOpt*, 54, 477,
 312 doi: [10.1364/AO.54.000477](https://doi.org/10.1364/AO.54.000477)
- 313 Bergren, M. S., Schuh, D., Sceats, M. G., & Rice, S. A.
 314 1978, *JChPh*, 69, 3477, doi: [10.1063/1.437080](https://doi.org/10.1063/1.437080)
- 315 Clark, C. D., & Crawford, J. H. 1973, *Advances in Physics*,
 316 22, 117, doi: [10.1080/00018737300101279](https://doi.org/10.1080/00018737300101279)
- 317 Cruikshank, D. P., Roush, T. L., Bartholomew, M. J., et al.
 318 1998, *Icarus*, 135, 389, doi: [10.1006/icar.1998.5997](https://doi.org/10.1006/icar.1998.5997)
- 319 Dumas, C., Merlin, F., Barucci, M. A., et al. 2007, *A&A*,
 320 471, 331, doi: [10.1051/0004-6361:20066665](https://doi.org/10.1051/0004-6361:20066665)
- 321 Gerakines, P. A., & Hudson, R. L. 2015, *ApJL*, 805, L20,
 322 doi: [10.1088/2041-8205/805/2/L20](https://doi.org/10.1088/2041-8205/805/2/L20)
- 323 —. 2020, *ApJ*, 901, 52, doi: [10.3847/1538-4357/abad39](https://doi.org/10.3847/1538-4357/abad39)
- 324 Grundy, W., Tegler, S., Steckloff, J., et al. 2023, *Icaurs*,
 325 doi: [10.1016/j.icarus.2023.115767](https://doi.org/10.1016/j.icarus.2023.115767)
- 326 Grundy, W. M., Schmitt, B., & Quirico, E. 2002, *Icarus*,
 327 155, 486, doi: [10.1006/icar.2001.6726](https://doi.org/10.1006/icar.2001.6726)
- 328 Grundy, W. M., Bird, M. K., Britt, D. T., et al. 2020,
 329 *Science*, 367, aay3705, doi: [10.1126/science.aay3705](https://doi.org/10.1126/science.aay3705)
- 330 Hagen, W., Tielens, A. G. G. M., & Greenberg, J. M. 1981,
 331 *Chemical Physics*, 56, 367,
 332 doi: [10.1016/0301-0104\(81\)80158-9](https://doi.org/10.1016/0301-0104(81)80158-9)
- 333 Hale, G. M., & Querry, M. R. 1973, *ApOpt*, 12, 555,
 334 doi: [10.1364/AO.12.000555](https://doi.org/10.1364/AO.12.000555)
- 335 Hansen, G. B. 1997, *J. Geophys. Res.*, 102, 21569,
 336 doi: [10.1029/97JE01875](https://doi.org/10.1029/97JE01875)
- 337 Hapke, B. 1993, *Theory of reflectance and emittance*
 338 *spectroscopy*
- 339 Heavens, O. 1991, *Optical Properties of Thin Solid Films*,
 340 2nd edn. (Addison-Wesley Professional)
- 341 Hobbs, P. V. 1974, *Ice physics*
- 342 Hudgins, D. M., Sandford, S. A., Allamandola, L. J., &
 343 Tielens, A. G. G. M. 1993, *ApJS*, 86, 713,
 344 doi: [10.1086/191796](https://doi.org/10.1086/191796)
- 345 Jenniskens, P., Blake, D. F., & Kouchi, A. 1998, in
 346 *Astrophysics and Space Science Library*, Vol. 227, *Solar*
 347 *System Ices*, ed. B. Schmitt, C. de Bergh, & M. Festou,
 348 139, doi: [10.1007/978-94-011-5252-5_7](https://doi.org/10.1007/978-94-011-5252-5_7)
- 349 Loeffler, M. J., Moore, M. H., & Gerakines, P. A. 2016,
 350 *ApJ*, 827, 98, doi: [10.3847/0004-637X/827/2/98](https://doi.org/10.3847/0004-637X/827/2/98)
- 351 Loeffler, M. J., Teolis, B. D., & Baragiola, R. A. 2006,
 352 *ApJL*, 639, L103, doi: [10.1086/502969](https://doi.org/10.1086/502969)
- 353 Loeffler, M. J., Tribbett, P. D., Cooper, J. F., & Sturmer,
 354 S. J. 2020, *Icarus*, 351, 113943,
 355 doi: [10.1016/j.icarus.2020.113943](https://doi.org/10.1016/j.icarus.2020.113943)
- 356 Lu, C.-S., & Lewis, O. 1972, *Journal of Applied Physics*,
 357 43, 4385, doi: [10.1063/1.1660931](https://doi.org/10.1063/1.1660931)
- 358 Mastrapa, R. M., Bernstein, M. P., Sandford, S. A., et al.
 359 2008, *Icarus*, 197, 307, doi: [10.1016/j.icarus.2008.04.008](https://doi.org/10.1016/j.icarus.2008.04.008)
- 360 Mastrapa, R. M., Sandford, S. A., Roush, T. L.,
 361 Cruikshank, D. P., & Dalle Ore, C. M. 2009, *ApJ*, 701,
 362 1347, doi: [10.1088/0004-637X/701/2/1347](https://doi.org/10.1088/0004-637X/701/2/1347)
- 363 Merlin, F., Barucci, M. A., de Bergh, C., et al. 2010, *Icarus*,
 364 208, 945, doi: [10.1016/j.icarus.2010.03.014](https://doi.org/10.1016/j.icarus.2010.03.014)
- 365 Molpeceres, G., Satorre, M. A., Ortigoso, J., et al. 2017,
 366 *MNRAS*, 466, 1894, doi: [10.1093/mnras/stw3166](https://doi.org/10.1093/mnras/stw3166)
- 367 Narten, A. H., Venkatesh, C. G., & Rice, S. A. 1976,
 368 *JChPh*, 64, 1106, doi: [10.1063/1.432298](https://doi.org/10.1063/1.432298)
- 369 Romanescu, C., Marschall, J., Kim, D., Khatiwada, A., &
 370 Kalogerakis, K. S. 2010, *Icarus*, 205, 695,
 371 doi: [10.1016/j.icarus.2009.08.016](https://doi.org/10.1016/j.icarus.2009.08.016)
- 372 Satorre, M. Á., Domingo, M., Millán, C., et al. 2008,
 373 *Planet. Space Sci.*, 56, 1748,
 374 doi: [10.1016/j.pss.2008.07.015](https://doi.org/10.1016/j.pss.2008.07.015)
- 375 Shkuratov, Y. G., Kreslavsky, M. A., Ovcharenko, A. A.,
 376 et al. 1999, *Icarus*, 141, 132, doi: [10.1006/icar.1999.6154](https://doi.org/10.1006/icar.1999.6154)
- 377 Tegler, S. C., Grundy, W. M., Olkin, C. B., et al. 2012,
 378 *ApJ*, 751, 76, doi: [10.1088/0004-637X/751/1/76](https://doi.org/10.1088/0004-637X/751/1/76)
- 379 Tempelmeyer, K. E., & Mills, D. W., J. 1968, *Journal of*
 380 *Applied Physics*, 39, 2968, doi: [10.1063/1.1656707](https://doi.org/10.1063/1.1656707)
- 381 Teolis, B. D., Loeffler, M. J., Raut, U., Famá, M., &
 382 Baragiola, R. A. 2007, *Icarus*, 190, 274,
 383 doi: [10.1016/j.icarus.2007.03.023](https://doi.org/10.1016/j.icarus.2007.03.023)
- 384 Tolstoy, V. P., Chernyshova, I., & Skryshesky, V. A. 2003,
 385 *Handbook of Infrared Spectroscopy of Ultrathin Films*
- 386 Westley, M. S., Baratta, G. A., & Baragiola, R. A. 1998,
 387 *JChPh*, 108, 3321, doi: [10.1063/1.475730](https://doi.org/10.1063/1.475730)